The Astrophysical Journal, 1002:20 (14pp), 2026 May 1 https://doi.org/10.3847/1538-4357/ae548a


# The Galaxy Activity, Torus, and Outflow Survey (GATOS). XIII. Coupling Driven $H_2$ Excitation in Seyferts

Daniel E. Delaney[1,2], Erin K. S. Hicks[1,2,3], Lulu Zhang[3], Ric Davies[4], Chris Packham[3], Rogemar A. Riffel[5], Miguel Pereira Santaella[6], Enrica Bellocchi[7,8], Nancy A. Levenson[9], Steph Campbell[10], David J. Rosario[10], Houda Haidar[10], Cristina Ramos Almeida[11,12], Anelise Audibert[11,12], Claudio Ricci[13,14], Laura Hermosa Muñoz[15], Francoise Combes[16], Almudena Alonso-Herrero[15], Santiago García-Burillo[17], Federico Esposito[17], Ismael García-Bernete[18], Taro Shimizu[4], Martin Ward[19], Omaira González-Martín[20], Alvaro Labiano[21], Oscar Veenema[22], Enrique Lopez-Rodriguez[23], Dimitra Rigopoulou[22,24], Marko Stalevski[25,26], Sebastian F. Hönig[27], Donaji Esparza-Arredondo[20], Takuma Izumi[28], Lindsay Fuller[3], and Daniel Rouan[29]
[1] Department of Physics, University of Alaska Fairbanks, Fairbanks, AK 99775, USA
[2] Department of Physics and Astronomy, University of Alaska Anchorage, Anchorage, AK 99508, USA
[3] Department of Physics and Astronomy, The University of Texas at San Antonio, 1 UTSA Circle, San Antonio, TX 78249, USA
[4] Max Planck Institute for Extraterrestrial Physics (MPE), Giessenbachstr. 1, 85748 Garching, Germany
[5] Departamento de Física, CCNE, Universidade Federal de Santa Maria, Av. Roraima 1000, 97105-900, Santa Maria, RS, Brazil
[6] Instituto de Física Fundamental, CSIC, Calle Serrano 123, 28006 Madrid, Spain
[7] Departamento de Física de la Tierra y Astrofísica, Fac. de CC. Físicas, Universidad Complutense de Madrid, 28040 Madrid, Spain
[8] Instituto de Física de Partículas y del Cosmos IPARCOS, Fac. CC. Físicas, Universidad Complutense de Madrid, 28040 Madrid, Spain
[9] Space Telescope Science Institute, Baltimore, MD, USA
[10] School of Mathematics, Statistics and Physics, Newcastle University, Newcastle upon Tyne, NE1 7RU, UK
[11] Instituto de Astrofísica de Canarias, Calle Vía Láctea, s/n, E-38205, La Laguna, Tenerife, Spain
[12] Departamento de Astrofísica, Universidad de La Laguna, E-38206, La Laguna, Tenerife, Spain
[13] Department of Astronomy, University of Geneva, ch. d'Ecogia 16, 1290, Versoix, Switzerland
[14] Instituto de Estudios Astrofísicos, Facultad de Ingeniería y Ciencias, Universidad Diego Portales, Av. Ejército Libertador 441, Santiago, Chile
[15] Centro de Astrobiología (CAB) CSIC-INTA, Camino Bajo del Castillo s/n, 28692, Villanueva de la Cañada, Madrid, Spain
[16] Observatoire de Paris, LUX, Collège de France, PSL Research University, CNRS, Sorbonne University, Paris, France
[17] Observatorio Astronómico Nacional (OAN-IGN)-Observatorio de Madrid, Alfonso XII, 3, 28014-Madrid, Spain
[18] Centro de Astrobiología (CAB), CSIC-INTA, Camino Bajo del Castillo s/n, E-28692 Villanueva de la Cañada, Madrid, Spain
[19] Centre for Extragalactic Astronomy, Department of Physics, Durham University, South Road, Durham, DH1 3LE, UK
[20] Instituto de Radioastronomía y Astrofísica (IRyA), Universidad Nacional Autónoma de México, Antigua Carretera a Pátzcuaro #8701, Colonia ExHda. San José de la Huerta, Morelia, Michoacán, C.P. 58089, México
[21] Telespazio UK for ESA, ESAC, Camino Bajo del Castillo s/n, 28692 Villanueva de la Cañada, Spain
[22] Department of Physics, University of Oxford, Keble Road, Oxford, OX1 3RH, UK
[23] Kavli Institute for Particle Astrophysics & Cosmology (KIPAC), Stanford University, Stanford, CA 94305, USA
[24] School of Sciences, European University Cyprus, Diogenes Street, Engomi, 1516 Nicosia, Cyprus
[25] Astronomical Observatory, Volgina 7, 11060 Belgrade, Serbia
[26] Sterrenkundig Observatorium, Universiteit Gent, Krijgslaan 281-S9, Gent B-9000, Belgium
[27] Department of Physics & Astronomy, University of Southampton, Highfield, Southampton SO171BJ, UK
[28] Department of Astronomy, School of Science, Graduate University for Advanced Studies (SOKENDAI), Mitaka, Tokyo 181-8588, Japan
[29] LESIA, Observatoire de Paris, Université PSL, CNRS, Sorbonne Université, Sorbonne Paris Cité, 5 place Jules Janssen, F-92195 Meudon, France
*Received 2026 January 21; revised 2026 February 18; accepted 2026 March 9; published 2026 April 22*

## Abstract

We utilize James Webb Space Telescope/Mid Infrared Instrument (JWST/MIRI) Integral Field Unit observations from the Galaxy Activity, Torus and Outflow Survey to investigate the diverse range of ionized outflow rates of obscured active galactic nuclei (AGN) with similar bolometric luminosity and explore potential associations with AGN feedback. We explore spatial correlations between ionized emission potentially associated with fast shocks ([Fe II]$_{5.34\mu m}$) and the excitation of $H_2$. We further constrain our investigation to the inner 400 pc (the nuclear and circumnuclear regions $r < 200$ pc), and estimate the excitation temperature and column density of $H_2$ assuming local thermodynamic equilibrium and using the S(1)–S(8) rotational $H_2$ emission lines visible to JWST/MIRI spectroscopy. We report the molecular gas temperature of the deprojected 400 pc nuclear region to correlate with the ionized mass outflow rate. We also observe a stronger degree of spatial correlation between [Fe II]$_{5.34\mu m}$ emission and $H_2$ gas temperature. We observe regions of enhanced [Fe II]$_{5.34\mu m}$/[Ar II]$_{6.99\mu m}$ spatially coincident with the ionization cones of objects with higher ionized outflow rates and [Fe II]$_{5.34\mu m}$/[Ar II]$_{6.99\mu m}$ in the deprojected 400 pc nuclear region to scale positively with both the ionized outflow rate and the estimated molecular gas temperature. We do not observe the estimated jet cavity power within the central 400 pc as strongly correlated with the ionized mass outflow rate or molecular gas temperature of the nuclear region. We take the preceding observations to suggest a higher degree of interaction between AGN outflows and the circumnuclear disk.

*Unified Astronomy Thesaurus concepts:* AGN host galaxies (2017); Active galaxies (17); Seyfert galaxies (1447); James Webb Space Telescope (2291)

## 1. Introduction

Large amounts of nonstellar radiation emanating from the Galactic center are the result of mass accretion around a galaxy's central supermassive black hole (SMBH). The high levels of energy associated with these active galactic nuclei (AGN) is thought to play an important role in galaxy evolution as these objects provide feedback from the growth of the SMBH to the rest of the galaxy (J. Silk & M. J. Rees 1998; A. Khalatyan et al. 2008; A. C. Fabian 2012; R. C. Hickox & D. M. Alexander 2018). Currently, our understanding of the anatomy of AGN is described by the AGN unified model (e.g., R. Antonucci 1993; C. M. Urry & P. Padovani 1995) in which the central SMBH is surrounded by a luminous accretion disk of thermo-viscous plasma and at larger scales surrounded by a dusty toroidal structure shrouding the AGN. The orientation and geometry of these components relative to the circumnuclear structures, such as the circumnuclear rotating disk, have implications for how the ionization bicone and outflowing material provide feedback to the host galaxy. While the interplay between the AGN and its host galaxy is complex (C. Ramos Almeida & C. Ricci 2017; C. M. Harrison & C. Ramos Almeida 2024), it remains a critical component in understanding galactic evolution. In fact, AGN activity is thought to regulate both the growth of the central SMBH itself (e.g., P. F. Hopkins et al. 2005), as well as impact large-scale galactic processes such as star formation via quenching (e.g., A. C. Fabian 2012; C. Cicone et al. 2014; C. Harrison et al. 2018) or enhancement (see R. Davies et al. 2007; P. Esquej et al. 2013; C. Harrison 2017; R. Maiolino et al. 2017; S. L. Ellison et al. 2018; P. S. Bessiere & C. Ramos Almeida 2022; J. Molina et al. 2023; L. Hermosa-Muñoz et al. 2024).

AGN-associated feedback can result from both radiative and kinetic processes and results in the redistribution of material and the provision of excitation energy (S. Veilleux et al. 2005; A. C. Fabian 2012; K. Wada 2012; S. Veilleux et al. 2013; C. Ramos Almeida & C. Ricci 2017; C. Harrison et al. 2018; S. García-Burillo et al. 2024). In addition to AGN-induced radiative heating, in Seyfert galaxies, components of the AGN outflows, such as radio jets and AGN winds (which have been shown to be relatively common; D. Crenshaw et al. 2010; T. Fischer et al. 2011; D. M. Crenshaw & S. B. Kraemer 2012; T. C. Fischer et al. 2018; R. A. Riffel et al. 2023), can provide kinetic feedback to the host galaxy. These kinetic mechanisms have the potential to induce shocks in the AGN circumnuclear region, destroying dust, heating, and disturbing gas (R. A. Riffel et al. 2025b). As such, it is reasonable to suspect that the relative geometry of AGN components (e.g., AGN ionization cone and circumnuclear disk coupling; C. Ramos Almeida et al. 2022) may regulate AGN feedback and behavior.

In this work, we utilize Integral Field Unit (IFU) observations from the James Webb Space Telescope (JWST; J. P. Gardner et al. 2023; J. Rigby et al. 2023) Mid Infrared Instrument (MIRI; G. H. Rieke et al. 2015) to investigate the excitation of $H_2$ in the circumnuclear region of six Seyferts (types 1.9 and 2) with a bolometric luminosity within an order of magnitude (in the range of $10^{43.4}$–$10^{44.3}$ erg s$^{-1}$) and similar distances, but we estimated ionized mass outflow rates ranging from 0.003 to 0.52 $M_\odot$ yr$^{-1}$ (derived from optical observation; R. Davies et al. 2020; 0.03 to 0.33 $M_\odot$ yr$^{-1}$; derived using observations in the mid-infrared (MIR; L. Zhang et al. 2024). These observations of otherwise similar objects presenting a wide range of ionized mass outflow rates highlight an important puzzle of AGN behavior, which must be solved to fully understand the role of the central SMBH engine in the host galaxy. Previously, it had been suggested that the range of observed ionized outflow rates, may be an artifact of differing relevant timescales of AGN luminosities ($\approx 10^4$–$10^5$ yr) and outflow properties ($\approx 10^6$ yr; K. Zubovas & E. Nardini 2020), or perhaps driven by geometric coupling between AGN outflows and the ambient disk promoting outflow mass loading and thereby bolstering the observed outflow rate (T. C. Fischer et al. 2016, 2018). In previous work (D. E. Delaney et al. 2025), we explored the excitation of $H_2$ in two Seyferts from the Galaxy Activity, Torus, and Outflow Survey (GATOS[30]) Cycle 1 sample (NGC 3081 and NGC 5506). We identified a differing suite of excitation mechanisms and AGN interactions with the circumnuclear $H_2$. For NGC 5506, we identified warm molecular gas entrained in the AGN outflow and suspected AGN-induced shock excitation to likely be an important excitation mechanism. Whereas for NGC 3081, AGN photoionization was sufficient to describe observations of the circumnuclear $H_2$. This work acts to extend this analysis of circumnuclear $H_2$ along the dimension of ionized outflow rate by incorporating the full GATOS Cycle 1 sample of six Seyferts at a fixed physical scale.

Utilizing the eight rotational emission lines visible to JWST/MIRI spectroscopy, we explore the spatial distribution of $H_2$ temperature and its distribution in relation to [Fe II]$_{5.34\mu m}$ (associated with shocks; B.-C. Koo et al. 2016; M. Pereira-Santaella et al. 2024; A. Alonso-Herrero et al. 2025), and map the distribution of [Fe II]$_{5.34\mu m}$ normalized by [Ar II]$_{6.99\mu m}$ (a primarily photoionized emission line; U. J. Sofia & E. B. Jenkins 1998; A. Verma et al. 2003; A. Amayo et al. 2021). In addition, we investigate the relationship between the observed ionized outflow rate and molecular gas temperature and [Fe II]$_{5.34\mu m}$/[Ar II]$_{6.99\mu m}$ of the nuclear region, as well as the estimated radio jet cavity power. We utilize methods similar to those used in previous studies that investigated $H_2$ gas population levels in a variety of objects, including ultra-luminous infrared galaxies, low-ionization nuclear emission-line regions, and Seyfert galaxies (see P. Ogle et al. 2007; M. Pereira-Santaella et al. 2014; A. Togi & J. Smith 2016; L. Zhang & L. C. Ho 2023; A. Alonso-Herrero et al. 2024; R. Davies et al. 2024; D. E. Delaney et al. 2025 and L. Hunt et al. 2025). This work acts to build upon previous studies that have investigated winds, feedback, and molecular outflows in local Seyferts. To highlight a few, interactions between AGN ionization cones and the circumnuclear disk have been identified by R. Davies et al. (2014), I. García-Bernete et al. (2024) and F. Esposito et al. (2024) and molecular outflows from a variety of AGN have been identified (e.g., J. F. Gallimore et al. 2016; M. Imanishi et al. 2018; A. Alonso-Herrero et al. 2019, 2023; C. V. Impellizzeri et al. 2019; S. García-Burillo et al.

[30] More information regarding the GATOS Collaboration and their ongoing research can be found at https://gatos.myportfolio.com/home.

**Table 1**
Fundamental Galaxy Parameters

| Galaxy | Host Type | AGN Type | $z$ | $D_L$ (Mpc) | $PA_{disk}$ (deg) | $i_{disk}$ (deg) | $PA_{cone}$ (deg) | $\Omega_{Out}$ (deg) | $\dot{M}_{out}$ ($M_\odot$ yr$^{-1}$) | log[$L_{AGN}$] (erg s$^{-1}$) | log[$L_{14-195\ keV}$] (erg s$^{-1}$) |
|---|---|---|---|---|---|---|---|---|---|---|---|
| (1) | (2) | (3) | (4) | (5) | (6) | (7) | (8) | (9) | (10) | (11) | (12) |
| ESO 137-G034 | SAB0/a | 2 | 0.00914 | 35 | 168 | 38 | 124 | 78 | 0.52; 0.33 | 43.4 | 42.77 |
| NGC 5506 | Sa pec | 1.9/1i | 0.00608 | 27 | 265 | 80 | 22 | 80 | 0.21; 0.28 | 44.1 | 43.31 |
| NGC 5728 | SAB(r)a | 1.9 | 0.00932 | 39 | 14 | 43 | 127 | 46 | 0.09; 0.08 | 44.1 | 43.26 |
| NGC 3081 | (R)SAB0/a(r) | 2 | 0.00798 | 34 | 75 | 41 | 165 | 30 | 0.04; 0.03 | 44.1 | 43.12 |
| NGC 7172 | Sa pec | 2 | 0.00868 | 37 | 90 | 88 | 2 | 120 | 0.005; 0.03 | 44.1 | 43.48 |
| MCG-05-23-016 | S0 | 2 | 0.00849 | 35 | 59 | 35 | 172 | — | 0.003; 0.04 | 44.3 | 43.54 |

**Note.** Columns (2)–(4) Host galaxy type, and object redshift, are taken from NASA/IPAC Extragalactic Database (NED); "*r*" and "*R*" indicate the presence of an inner or outer ring, respectively. Column (5) Object distances are taken from T. Caglar et al. (2020). Column (6) References for the position angle of the circumnuclear rotational disk for ESO 137-G034 taken from L. Zhang et al. (2024); NGC 5506 taken from F. Esposito et al. (2024); NGC 5728 taken from T. T. Shimizu et al. (2019); NGC 3081 taken from D. Ruschel-Dutra et al. (2021); NGC 7172 taken from A. Alonso-Herrero et al. (2023); MCG-05-23-016 taken from D. Esparza-Arredondo et al. (2025). Column (7) Inclination of the circumnuclear disk for ESO 137-G034 taken from L. Burtscher et al. (2021); NGC 5506 taken from F. Esposito et al. (2024); NGC 5728 taken from T. T. Shimizu et al. (2019); NGC 3081 taken from L. Burtscher et al. (2021); NGC 7172 taken from A. Alonso-Herrero et al. (2023); MCG-05-23-016 taken from D. Esparza-Arredondo et al. (2025). Column (8) Position angle of the ionization cone for ESO 137-G034 taken from L. Zhang et al. (2024); NGC 5506 taken from T. Fischer et al. (2013); NGC 5728 taken from L. Zhang et al. (2024); NGC 3081 taken from L. Zhang et al. (2024); NGC 7172 taken from A. Alonso-Herrero et al. (2023); MCG-05-23-016 taken from L. Zhang et al. (2024). Column (9) Ionization cone opening angle for ESO 137-G034 taken from J. Ma et al. (2020); NGC 5506 taken from T. Fischer et al. (2013); NGC 5728 taken from T. T. Shimizu et al. (2019); NGC 3081 taken from A. Schnorr-Müller et al. (2016); NGC 7172 taken from A. Alonso-Herrero et al. (2023); MCG-05-23-016, no information available. Column (10) Estimated ionized mass outflow rates are from R. Davies et al. (2020); L. Zhang et al. (2024). Column (11) AGN bolometric luminosity from R. Davies et al. (2020). Column (12) 14–195 keV X-ray luminosity taken from the 157-month Swift-BAT survey A. Y. Lien et al. (2025).

2014, 2016, 2019, 2021; I. García-Bernete et al. 2021, 2024; D. E. Delaney et al. 2025; M. Imanishi et al. 2025).

The organization of this paper is as follows: In Section 2, we present the sample selection and describe the data collection and reduction process. In Section 3, we present the spatial distribution and molecular gas temperature, ionized, and radio emission. In Section 4, we explore the molecular gas temperature (Section 4.1), [Fe II]$_{5.34\mu m}$/[Ar II]$_{6.99\mu m}$ (Section 4.2), and radio jet cavity power (Section 4.3) of the deprojected 400 pc nuclear region ($r < 200$ pc). Finally, we provide a summary of results in Section 5. Additional information regarding the sample, methodology, and background information is presented in the Appendix.

## 2. Sample and Observations

The GATOS Collaboration observed six nearby AGN in the MIR as part of the JWST Cycle 1 program 1670 (PI: T. Shimizu). Targets (Table 1) were selected from the R. I. Davies et al. (2015) sample, who identified objects in the 70 month Swift-Burst Alert Telescope (BAT) All-sky Hard X-ray Survey (W. Baumgartner et al. 2013) as ideal candidates to investigate the behavior of AGN outflows. The GATOS Cycle 1 sample is designed to explore differences in ionized mass outflow rates: galaxies within the sample span a narrow range of key parameters but present a wide range of observed ionized outflow rates. The sample is distance limited (<40 Mpc) and all objects have bolometric luminosities within an order of magnitude (in the range of $10^{43.4}$–$10^{44.3}$ erg s$^{-1}$) but with outflow rates spanning 2 orders of magnitude (R. Davies et al. 2020; L. Zhang et al. 2024). In addition, these targets are of similar AGN type (Seyfert types 1.9 and 2), and host galaxies in the sample include three lenticular and three spiral galaxies. To this date, numerous studies have been conducted utilizing the GATOS Cycle 1 sample set and analyzing each individual target. In Appendix A.1, we provide a brief overview of each target and potential evidence for strong/weak outflow–disk coupling.

### 2.1. Data Collection

This study utilizes MIR Integral Field Unit (IFU) observations from the Mid Infrared Instrument (MIRI; G. H. Rieke et al. 2015) on board JWST. JWST/MIRI is capable of performing medium resolution spectroscopy (MRS; M. Wells et al. 2015; I. Argyriou et al. 2023) between 4.9 and 27.9 μm (M. Wells et al. 2015; I. Argyriou et al. 2023). Data cubes were processed via the standard calibration pipeline (version 1.11.4) and supplemented with some additional steps masking erroneously hot and cold pixels, which were not identified by the standard data reduction pipeline. The data reduction process is described in detail in M. Pereira-Santaella et al. (2022), I. García-Bernete et al. (2024), and I. García-Bernete et al. (2022).

## 3. Distribution of Molecular Excitation

In optically thin gas, the observed line flux is directly proportional to the number of emitting particles. Assuming a Boltzmann's distribution, the temperature of a gas can be calculated from the observed flux ratio of two rotational hydrogen lines with corresponding energies $E_i$ and $E_j$,

$$T = \frac{E_j - E_i}{k \cdot \ln\left(\frac{g_j A_j \lambda_i F_i}{g_i A_i \lambda_j F_j}\right)} \quad (1)$$

where $E_i$ and $E_j$ are the energy level corresponding to states $i$ and $j$, respectively, $k$ is the Boltzmann constant, $F_i$ is the observed total flux, $\lambda_i$ is the frequency of emission, $A_i$ is the probability of transition, and $g_i$ is the degeneracy value associated with the given state denoted by $i$ (or $j$, respectively).

Using the $H_2$ 0-0 S(1)/S(5) line flux ratio (line fitting described in Appendix A.2), we map the temperature of $H_2$ for each object within the sample (Figure 1). The molecular gas temperature is centrally peaked near the AGN for each object, but the extended morphology varies. The three objects with the highest ionized outflow rates (ESO 137-G034, NGC 5506, and

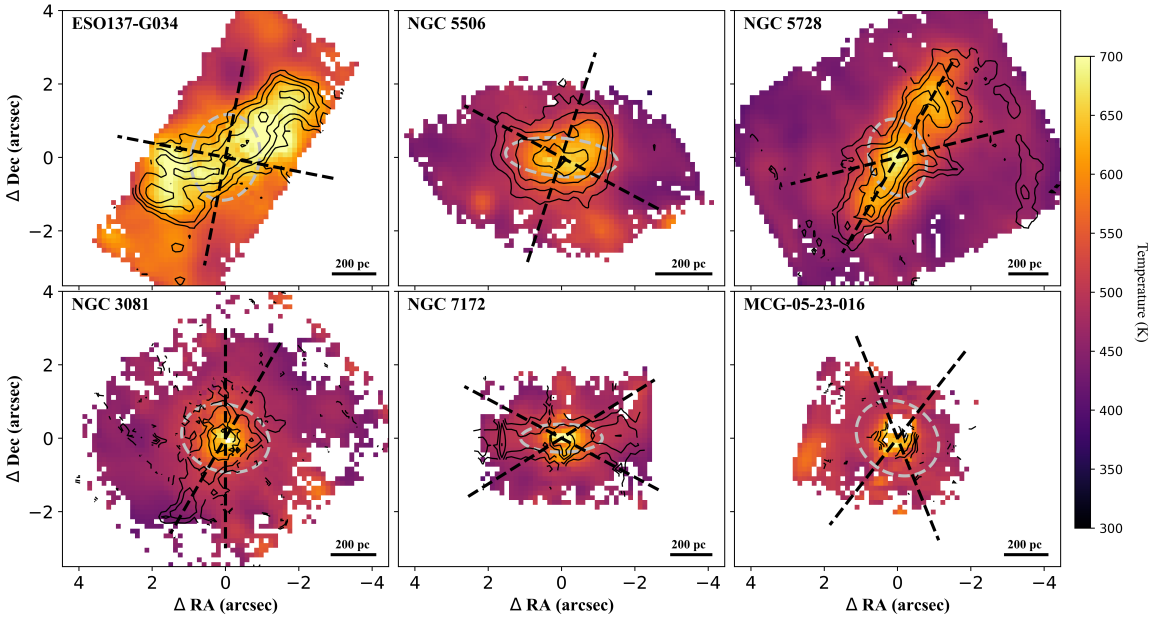


**Figure 1.** $H_2$ excitation temperature mapping for each object derived from the $H_2$ 0-0 S(1)/S(5) line ratio. Panels are presented with estimated ionized mass outflow rate decreasing from top to bottom and left to right, with the highest ionized outflow rate in the top left (ESO 137-G034) and the lowest in (MCG-05-23-16) in the bottom right. The dashed black line indicates the edges of the ionization bicone (see Table 1). The gray ellipse represents a deprojected aperture of the central 400 pc ($r = 200$ pc). For MCG-05-23-016, since no information on the opening angle is available, a default of 60° has been used. Black contours represent the [Fe II]$_{5.34\mu m}$ flux contours ranging from $10^{-16.45}$ to $10^{-15.7}$ erg s$^{-1}$ cm$^{-2}$ (0.25 dex steps) for ESO 137-34, $10^{-15.95}$ to $10^{-15.2}$ erg s$^{-1}$ cm$^{-2}$ (0.25 dex steps) for NGC 5506, $10^{-16.7}$ to $10^{-15.95}$ erg s$^{-1}$ cm$^{-2}$ (0.25 dex steps) for NGC 5728, $10^{-17.2}$ to $10^{-16.45}$ erg s$^{-1}$ cm$^{-2}$ (0.25 dex steps) for NGC 3081, $10^{-16.6}$ to $10^{-15.85}$ erg s$^{-1}$ cm$^{-2}$ (0.25 dex steps) for NGC 7172, and $10^{-17.2}$ to $10^{-16.45}$ erg s$^{-1}$ cm$^{-2}$ (0.25 dex steps) for MCG-05-23-016. The gray dashed regions depict the nuclear aperture investigated in Section 4.

NGC 5728) show an extension aligned with the ionization cones of each object, whereas for the three objects with lower ionized outflow rates (NGC 3081, NGC 7172, and MCG-05-23-016), we see a more centrally concentrated temperature distribution. This suggests a potential connection between the ionization cone and extended $H_2$ excitation for objects presenting increased ionized outflow rates.

### 3.1. $H_2$ Temperature Distributions

Overlain on the temperature maps for each object (Figure 1), we include the emission contours for [Fe II]$_{5.34\mu m}$. Iron emission can result from photoionization, but is expected to be enhanced by shock-induced dust destruction (B.-C. Koo et al. 2016; M. Pereira-Santaella et al. 2024; R. A. Riffel et al. 2025b). Dust destruction resulting from shattering and sputtering in shocked environments is understood to release refractory elements such as iron that were previously trapped within dust grains (A. Jones et al. 1994, 1996; A. Tielens et al. 1994). This association with shocks makes iron ionized emission of particular interest, and we therefore utilize it to trace potentially AGN-driven excitation.

Qualitatively speaking, the three objects in the sample with the highest ionized outflow rates (ESO 137-G034, NGC 5506, and NGC 5728) show similar elongation and distribution of $H_2$ temperature and [Fe II]$_{5.34\mu m}$ emission (Figure 1). The distribution of increased temperature and [Fe II]$_{5.34\mu m}$ emission in these targets is spatially coincident with the ionization cones of each respective target, although the perceived alignment with the cone varies. In the case of NGC 5728 and NGC 5506, these features track along one or both of the edges of the ionization cone, tempting us to speculate that these correlations manifest where the ionization cone intersects the circumnuclear disk. For ESO 137-G034, however, these extended features appear to bisect the opening angle of the ionization cone and reside primarily within the cone itself. It could be the case that these correlations exist independent of the relative geometry between the ionization cone and the circumnuclear disk, or this could be an artifact of our line-of-sight viewing of the ionization cone and the circumnuclear disk, with interaction between the cone and disk occurring on the farside of the cone. More detailed geometric modeling of the circumnuclear disk and ionization cone is needed to fully assess this.

For NGC 3081, NGC 7172, and MCG-05-23-016, targets presenting lower ionized outflow rates, the temperature distribution is more centrally concentrated, and [Fe II]$_{5.34\mu m}$ emission is not as clearly correlated with molecular gas temperature. We observe some extension of [Fe II]$_{5.34\mu m}$ emission for NGC 3081 along the southeast portion of the ionization bicone; however, this extension is not clearly observed in the $H_2$ temperature distribution, potentially suggesting different excitation mechanisms. For NGC 7172, we observe extension of [Fe II]$_{5.34\mu m}$ emission along the circumnuclear disk perpendicular to the direction of the ionization bicone. We interpret this emission to likely result from the star-forming ring present within the circumnuclear region of the galaxy (L. Hermosa-Muñoz et al. 2024).

To quantify the spatial correlation between the ionized [Fe II]$_{5.34\mu m}$ emission distribution and the molecular gas temperature, we calculate both the Sørensen–Dice coefficient (SDC) and the Pearson coefficient ($\rho$). SDC, which aims to quantify the spatial overlap between the two distributions, for

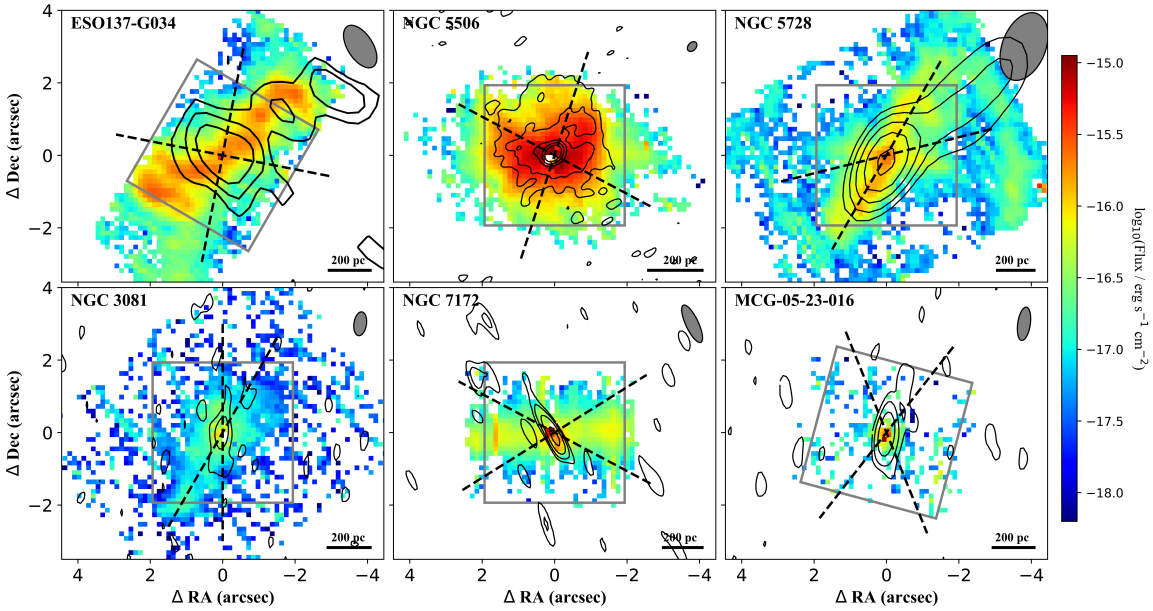


**Figure 2.** [Fe II]$_{5.34\mu m}$ emission maps for each target. The black contours overlain on flux maps present the observed radio intensity for each object. The dashed black lines represent the edges of each target's ionization bicone. For MCG-05-23-016, since no information on the opening angle is available, a default of 60° has been used. For ESO 137-G034, the 8 GHz radio contour intervals (R. Morganti et al. 1999) range from $10^{-3.5}$ to $10^{-3.0}$ Jy beam$^{-1}$ with a 0.25 dex step. For NGC 5506, the 8.46 GHz radio contour intervals (H. Schmitt et al. 2001) range from $10^{-4.5}$ to $10^{-2.0}$ Jy beam$^{-1}$ with a 0.5 dex step. For NGC 5728, the 4.9 GHz radio contour intervals (H. Schmitt et al. 2001) range from $10^{-3}$ to $10^{-2.4}$ Jy beam$^{-1}$ with a 0.15 dex step. For NGC 3081, the 4.9 GHz radio emission contour intervals (NRAO/Very Large Array (VLA) Archive Survey 2007) from $10^{-4.0}$ to $10^{-2.0}$ Jy beam$^{-1}$ with a 0.5 dex step. For NGC 7172, the 4.9 GHz radio emission contour intervals (NRAO/VLA Archive Survey 2007) from $10^{-3.75}$ to $10^{-3.0}$ Jy beam$^{-1}$ with a 0.25 dex step. For MCG-05-23-016, the 4.9 GHz radio emission contour intervals (NRAO/VLA Archive Survey 2007) from $10^{-3.75}$ to $10^{-2.75}$ Jy beam$^{-1}$ with a 0.5 dex step. The gray ellipse in the top right corner of each panel indicates the respective beam size. The gray square aperture represents the region used for the computation of the Sørensen–Dice and Pearson coefficients.

two positive normalized arrays can be calculated as

$$\mathrm{SDC} = 1 - \frac{\sum^i\sum^j |Y_{i,j} - X_{i,j}|}{\sum^i\sum^j (|X_{i,j}| + |Y_{i,j}|)} \quad (2)$$

where $Y$ and $X$ are the respective flux maps being compared. $\rho$, which quantifies the linear covariance, is computed as

$$\rho = \frac{\sum^i\sum^j (X_{i,j} - \overline{X})(Y_{i,j} - \overline{Y})}{\sqrt{\sum^i\sum^j (X_{i,j} - \overline{X})^2}\sqrt{\sum^i\sum^j (Y_{i,j} - \overline{Y})^2}} \quad (3)$$

where $Y$ and $X$ are the respective flux maps being compared, and $\overline{Y}$ and $\overline{X}$ are the average values of the flux map. Each of these quantities ranges from 0 to 1, with higher values indicating stronger levels of spatial overlap and covariance, respectively. To ensure similar spatial scaling and resolution, the [Fe II]$_{5.34\mu m}$ emission map was convolved with the FWHM of the $H_2$ 0-0 S(1) (17.0346 $\mu$m) point-spread function (PSF), and we compute these values for 15″ nuclear apertures (indicated by gray square in Figure 2). Additionally, to mitigate scaling effects, both maps were normalized by the maximum value of each respective map. For these calculations, any spaxels that were masked as nondetections were given a value of zero. Figure 3 presents both the calculated SDC and $\rho$ as it relates to the ionized outflow rate. The strength of the spatial correlation between [Fe II]$_{5.34\mu m}$ and $H_2$ temperature distribution, via the SDC and $\rho$, scales with ionized outflow rate. The higher spatial correlation between [Fe II]$_{5.34\mu m}$ and temperature is suggestive of a shared excitation mechanism between molecular gas and iron.

### 3.2. [Fe II]$_{5.34\mu m}$/[Ar II]$_{6.99\mu m}$ Distributions

Of course, [Fe II]$_{5.34\mu m}$ emission is insufficient to conclude the presence of shocks as it can also result from photoionization and is only enhanced by dust destruction. Unlike iron, which is depleted into dust (E. B. Jenkins 2009), argon is a noble gas with a large photoionization cross section and low condensation temperature with respect to iron (Ar: 48 K; Fe: 1334 K; see K. Lodders 2003). As such, it is not anticipated to suffer significant dust depletion (U. J. Sofia & E. B. Jenkins 1998; A. Verma et al. 2003; A. Amayo et al. 2021) and will not be significantly enhanced by shock-induced dust destruction, making it a useful tracer for baseline photoionization (see R. A. Riffel et al. 2025b). To identify regions of potential shocks, we therefore look for enhancements of [Fe II]$_{5.34\mu m}$ with respect to [Ar II]$_{6.99\mu m}$. Figure 4 presents the [Fe II]$_{5.34\mu m}$/[Ar II]$_{6.99\mu m}$ flux ratio maps for each target in the sample. For the three targets with the lowest ionized outflow rates (NGC 3081, NGC 7172, and MCG-05-23-016), we observe a relatively uniform distribution of [Fe II]$_{5.34\mu m}$/[Ar II]$_{6.99\mu m}$. This is in stark contrast to the targets of the highest observed ionized outflow rates, in which we observe regions of elevated [Fe II]$_{5.34\mu m}$ emission, particularly in areas spatially coincident with the ionization bicone.

Notably, regions with the most significant increase in [Fe II]$_{5.34\mu m}$/[Ar II]$_{6.99\mu m}$ are at a distance from the AGN rather than immediately surrounding the AGN. This may be a result of the immediate nuclear region being partially cleared of dust due to the harsh radiative field of the AGN, which enhances both [Ar II]$_{6.99\mu m}$ and [Fe II]$_{5.34\mu m}$ emission, or perhaps an artifact of AGN-driven photoionization being less significant at a distance from the AGN. It could be that as the ionization cone or AGN outflows interact with the ambient

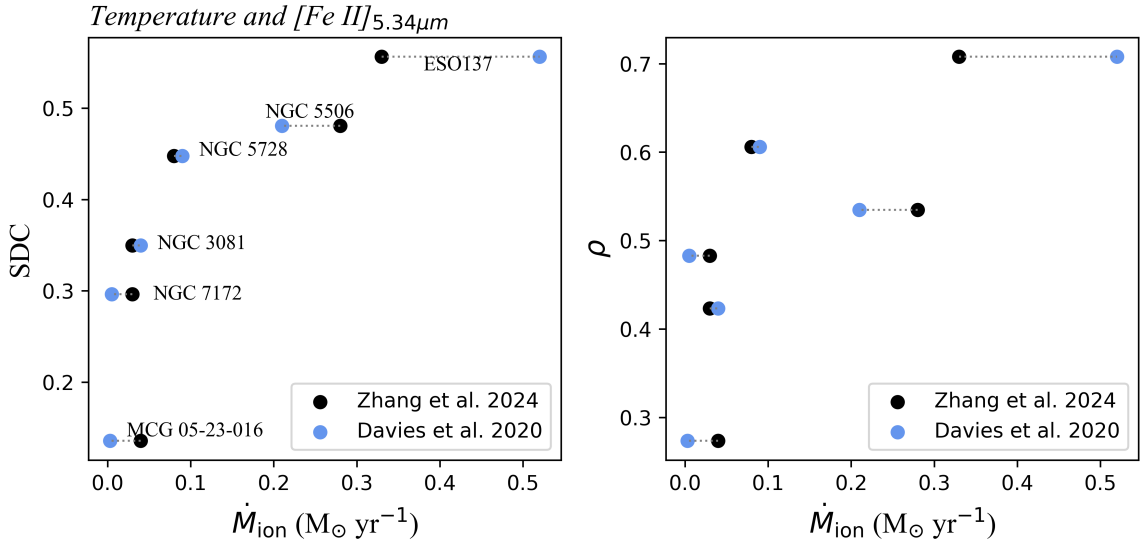


**Figure 3.** Dice coefficient (left panel) and Pearson coefficient (right panel) calculated from the $H_2$ excitation map and [Fe II]$_{5.34\mu m}$ emission map vs. the ionized outflow rate of each target.

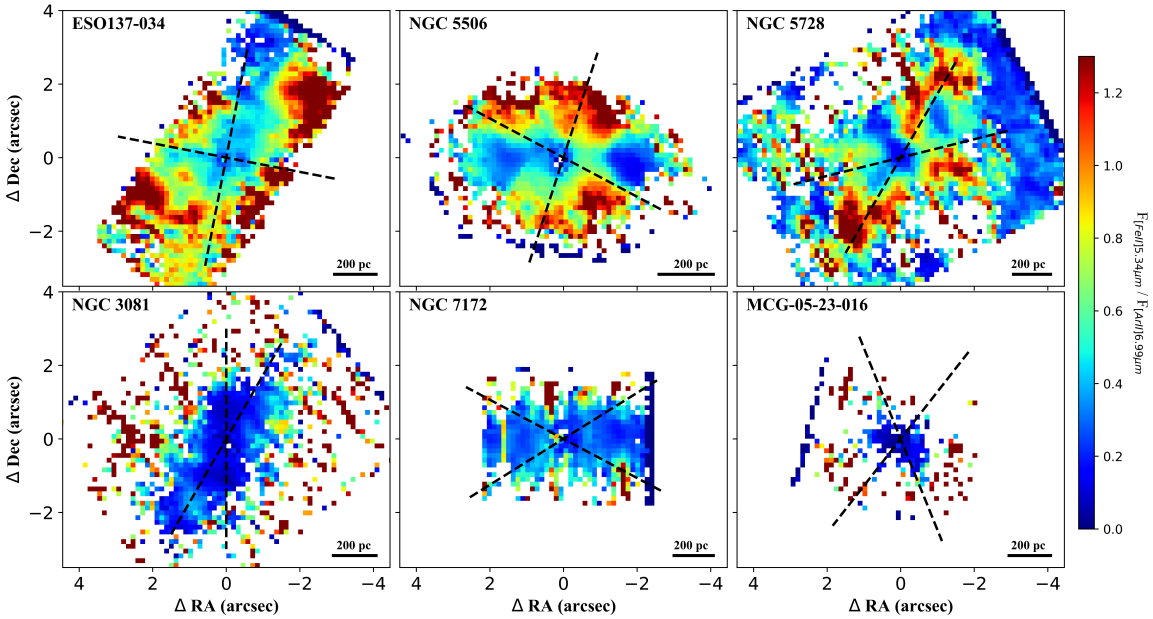


**Figure 4.** [Fe II]$_{5.34\mu m}$/[Ar II]$_{6.99\mu m}$ map vs. the ionized outflow rate of each target. Panels are presented with estimated ionized mass outflow rate increasing from top to bottom and left to right, with the highest ionized outflow rate in the top left (ESO 137-G034) and the lowest (MCG-05-23-16) in the bottom right. Here, the [Fe II]$_{5.34\mu m}$ map has been convolved with the FWHM of the [Ar II]$_{6.99\mu m}$ PSF to match spatial scales. The dashed black line indicates the edges of the ionization bicone (see Table 1). For MCG-05-23-016, since no information on the opening angle is available, a default of 60° has been used.

interstellar medium (ISM), dust is destroyed and [Fe II]$_{5.34\mu m}$ is enhanced independent of [Ar II]$_{6.99\mu m}$. As discussed in Section 3.1, these regions of enhanced [Fe II]$_{5.34\mu m}$/[Ar II]$_{6.99\mu m}$ may manifest where the ionization cone interacts with the circumnuclear disk, and modeling to constrain the relative geometries of the disk and outflow in each galaxy is needed to explore this further. Enhancement along the edge of the ionization cone rather than throughout the center of the cone, where AGN photoionization is expected to be significant, as is particularly clear for NGC 5728, supports this hypothesis and may be evidence that this enhancement results from shocks destroying dust at the interaction between the cone and disk. However, it is difficult to quantify the fraction of shock contribution to the observed [Fe II]$_{5.34\mu m}$ emission. Recent theoretical models (L. Zhang et al. 2025, see their Figure 8) find that in fast radiative shock environments [Fe II]$_{5.34\mu m}$/[Ar II]$_{6.99\mu m}$ ratios of greater than 10 are predicted. While the sample galaxies display lower ratios throughout their circumnuclear regions, suggesting that AGN photoionization is the dominant excitation mechanism, it is still possible that fast radiative shocks are present, and to some degree, contribute to excitation and result in enhancing

[Fe II]$_{5.34\mu m}$ emission. Alternatively, it could be that slower shocks driven by AGN winds or outflows may be responsible for the enhanced line ratio in these regions. In Section 4.2, we explore [Fe II]$_{5.34\mu m}$/[Ar II]$_{6.99\mu m}$ for the nuclear region directly.

### 3.3. Radio Emission

Radio emission has been shown to be a tracer of AGN feedback and may correlate with shock excitation as jets impact ambient gas and drive AGN outflows (C. Ramos Almeida et al. 2022; A. Audibert et al. 2023; L. P. de Arriba et al. 2023; I. García-Bernete et al. 2024; L. R. Holden et al. 2024). In fact, G. Venturi et al. (2021) showed that the ionized gas mass and gas kinetic energy correlate with jet power in four Seyfert AGN. In recent work, R. A. Riffel et al. (2025) concluded that excess $H_2$ emission in kinematically disturbed regions is induced by shocks driven by radio jets interacting with the ISM. Figure 2 presents the [Fe II]$_{5.34\mu m}$ emission distribution and radio intensity distribution for each target. For the three targets with the highest ionized outflow rates, we observe elongation of radio emission coincident with the distribution of [Fe II]$_{5.34\mu m}$ emission (and by extension the distribution of $H_2$ excitation; Figure 1). For ESO 137-G034 and NGC 5728, the elongation of the jet is primarily along the northwestern ionization cone and does not present the same extension along the southeastern ionization cone. Whether it be AGN radio jets impacting and shocking circumnuclear gas and dust, or shocked gas from AGN winds/outflows ionizing and producing synchrotron radiation (e.g., N. L. Zakamska & J. E. Greene 2014; T. Fischer et al. 2019; T. C. Fischer et al. 2023), we take this as further evidence that AGN activity plays an important role in molecular gas excitation in the three objects with the highest ionized outflow rates (ESO 137-G034, NGC 5506, and NGC 5728).

## 4. The Central 400 Parsecs

In an effort to apply uniform treatment over consistent spatial scales, we focus our analysis on the $H_2$ within the central deprojected 400 pc (deprojected nuclear radii $r < 200$ pc) (Figure 1 gray apertures). This spatial scale was selected to ensure adequate signal to noise and to ensure a region at least as large as the PSF FWHM at the longest wavelength. To better constrain our analysis to the circumnuclear rotational disk, the nuclear apertures have been adjusted to match the inclination and position angle of the rotational disk circumnuclear to the AGN for each respective target (Table 1). For NGC 3081 and ESO 137-G034, the geometry of the circumnuclear region is not well constrained, and thus, we assume the circumnuclear disk at these scales matches that of the disk at larger scales reported in L. Burtscher et al. (2021). For NGC 5506 and NGC 7172, which are highly inclined (80° and 88°, respectively), the aperture inclination has been limited to 70° to ensure that the aperture is not smaller than the PSF FWHM.

From the extracted integrated spectra (Appendix A.3, Figure 6), we measure line fluxes for the $H_2$ 0-0 S(1)–S(8) rotational emission lines visible to JWST MIRI/MRS and estimate the associated population levels ($N_i/g_i$) following the methodology outlined in detail in D. E. Delaney et al. (2025). Measured line fluxes for each target are presented in the top panel of Table 2. Prior to computation of individual population levels, we have adjusted flux measurements for the extinction between rotational emission lines (details provided in Appendix A.4). Assuming local thermodynamic equilibrium (LTE), where the warm $H_2$ is expected to be primarily thermalized, we follow the procedure of A. Togi & J. Smith (2016), in which the distribution of $H_2$ density with temperature follows a single power law (SPL), such that

$$dN \propto T^{-\beta} dT \tag{4}$$

where $dN$ is the differential change in column density, and $\beta$ is the power-law index, which relates the proportions of warm to cool molecular gas mass. We compare our measured population levels for the eight measured rotational $H_2$ emission lines to obtain the best-fit free parameters for the LTE model ($N_{tot}$ and $\beta$) for the temperature range of 200–2000 K. The lower limit of 200 K is employed, as for a thermalized gas at temperatures above this threshold, an ortho–para hydrogen ratio of 3 can safely be assumed (M. G. Burton et al. 1992). Immediately adjacent to the $H_2$ 0-0 S(7) emission line is the coronal emission line [Mg VII]$_{5.503\mu m}$, which can be prevalent in the nuclear region around AGN. In some cases, the $H_2$ 0-0 S(7) emission is blended with [Mg VII]$_{5.503\mu m}$ and difficult to deblend; we therefore omit the S(7) associated population level from our model fit but still present the measured line fluxes and population level with the caveat of potential contamination.

As Equation (4) describes the particle column density as a function of temperature, we can obtain the population mean temperature from the LTE model best fit via

$$<T> = \frac{\int_{T_l}^{T_u} T \cdot T^{-\beta} dT}{\int_{T_l}^{T_u} T^{-\beta} dT} \tag{5}$$

where $T_l = 200$ K and $T_u = 2000$ K. For redundancy, we employ a second methodology and compute the isothermal gas temperature using the integrated $H_2$ 0-0 S(1)/S(5) line flux ratio (Equation (1)). Model best-fit parameters and gas excitation temperatures are presented in Table 2. Population levels and SPL best-fit results are presented in Appendix A.3, Figure 7.

### 4.1. Excitation and Ionized Mass Outflow Rate

For this analysis, we compare our observations to ionized mass outflow rates estimated using two different methodologies: R. Davies et al. (2020), who used the optical [O III] luminosity, and more recently, L. Zhang et al. (2024) used the MIR line [Ne V]$_{14.322\mu m}$. Figure 5 (top panels) presents the measured $H_2$ gas temperature estimated via the S(1)/S(5) line ratio, the population mean temperature estimated from the SPL modeling results, and the estimated column density from the LTE modeling. Temperature estimates derived from the SPL-LTE modeling are lower than those from the S(1)/S(5) line ratio, as rather than assuming a single gas temperature, the SPL-LTE modeling assumes a distribution of particles with most of the molecular mass occupying lower energy states (i.e., cooler gas).

We observe a positive correlation between the ionized outflow rate and both the S(1)/S(5) derived gas temperature and the population mean temperature derived from the SPL-LTE model. This suggests that additional excitation energy is imparted onto the $H_2$ of the circumnuclear region around AGN

**Table 2**
Measured $H_2$ 0-0 S(1)–S(8), [Fe II]$_{5.34\mu m}$, [Ar II]$_{6.99\mu m}$, Emission Line Flux from the 400 pc Nuclear Apertures of Each Respective Target, Where a Reliable Line Fit Was Achieved

| Emission Line | $\lambda_{rest}$ | Deprojected $r < 200$ pc Nuclear Line Flux ($10^{-16}$ erg s$^{-1}$ cm$^{-2}$)[a] | | | | | |
|---|---|---|---|---|---|---|---|
| | ($\mu$m) | ESO 137-G034 | NGC 5506 | NGC 5728 | NGC 3081 | NGC 7172 | MCG-05-23-16 |
| (1) | (2) | (3) | (4) | (5) | (6) | (7) | (8) |
| $H_2$ 0-0 S(1) | 17.035 | 104.3 ± 2.5 | 233.1 ± 6.2 | 155.0 ± 1.4 | 113.0 ± 1.5 | 46.2 ± 0.7 | 100.2 ± 3.6 |
| $H_2$ 0-0 S(2) | 12.279 | 83.6 ± 0.5 | 179.7 ± 2.6 | 113.1 ± 1.0 | 58.4 ± 1.5 | 28.8 ± 1.3 | 56.7 ± 5.4 |
| $H_2$ 0-0 S(3) | 9.6649 | 275.6 ± 0.6 | 243.6 ± 1.9 | 194.3 ± 1.6 | 160.9 ± 0.6 | 20.9 ± 0.4 | 130.3 ± 1.3 |
| $H_2$ 0-0 S(4) | 8.0251 | 123.0 ± 0.5 | 183.6 ± 3.0 | 136.9 ± 0.9 | 62.1 ± 0.8 | 33.0 ± 1.4 | 41.6 ± 1.1 |
| $H_2$ 0-0 S(5) | 6.9095 | 286.9 ± 1.5 | 498.7 ± 3.3 | 300.6 ± 1.7 | 139.0 ± 1.6 | 71.4 ± 1.6 | 100.3 ± 2.3 |
| $H_2$ 0-0 S(6) | 6.1086 | 58.2 ± 0.4 | 102.4 ± 2.3 | 65.7 ± 0.5 | 24.2 ± 0.6 | …[b] | 21.3 ± 1.8 |
| $H_2$ 0-0 S(7)[c] | 5.5112 | 107.5 ± 5.7 | 300.2 ± 4.0 | 229.8 ± 3.8 | 90.8 ± 3.6 | 41.5 ± 1.1 | 56.4 ± 0.0 |
| $H_2$ 0-0 S(8) | 5.053 | 32.7 ± 0.3 | 69.9 ± 4.4 | 36.3 ± 0.5 | 20.4 ± 1.0 | 9.7 ± 1.0 | 13.8 ± 1.2 |
| [Fe II] | 5.34 | 214.1 ± 0.7 | 848.5 ± 4.5 | 122.8 ± 0.4 | 32.8 ± 0.5 | 64.5 ± 0.8 | 38.1 ± 0.5 |
| [Ar II] | 6.985 | 486.2 ± 1.7 | 2231.9 ± 13.0 | 380.6 ± 3.6 | 286.9 ± 0.6 | 245.0 ± 2.0 | 591.3 ± 1.4 |
| | | | | Radio Power | | | |
| log[$L_{1.4GHz}$ W Hz$^{-1}$] | | 22.3 | 22.8 | 22.9 | 21.6 | 22.0 | 22.6 |
| log[$P_{cav}$ W Hz$^{-1}$][d] | | 25.3 ± 0.02 | 25.4 ± 0.01 | 25.5 ± 0.02 | 25.0 ± 0.07 | 25.1 ± 0.04 | 25.4 ± 0.0001 |
| | | | | S(5)/S(1) Derived Gas Temperature[e] | | | |
| Temperature (K) | | 645.3 ± 2.9 | 606.8 ± 3.0 | 597.6 ± 1.1 | 562.3 ± 1.6 | 562.3 ± 2.6 | 546.4 ± 3.7 |
| | | | | LTE Fit Parameters[f] | | | |
| $\beta$ | | 3.83 ± 0.15 | 4.04 ± 0.11 | 4.12 ± 0.12 | 4.43 ± 0.18 | 4.26 ± 0.11 | 4.53 ± 0.12 |
| log[$N_{H_2}$ cm$^{-2}$] | | 20.7 ± 0.1 | 21.2 ± 0.1 | 21.1 ± 0.1 | 20.7 ± 0.1 | 20.9 ± 0.1 | 20.6 ± 0.06 |
| log[$M_{H_2}/M_\odot$] | | $5.85^{+0.71}_{-0.79}$ | $6.07^{+0.86}_{-0.92}$ | $6.23^{+0.81}_{-0.88}$ | $5.88^{+0.66}_{-0.75}$ | $5.78^{+0.90}_{-0.95}$ | $5.85^{+0.86}_{-0.92}$ |
| Average temperature (K) | | 305.3 ± 7.0 | 295.8 ± 4.5 | 292.5 ± 4.6 | 281.4 ± 5.2 | 287.2 ± 3.9 | 278.3 ± 3.3 |

**Notes.** The 1.4 GHz monochromatic radio luminosity of the 400 pc nuclear aperture and estimated jet cavity power within this same aperture. $H_2$ 0-0 S(1)/S(5) derived excitation temperature, LTE model best-fit parameters, as well as total estimate molecular mass within each aperture, are also presented.
[a] Flux values presented do not have extinction corrections applied.
[b] Due to a noisy continuum and potential blending with an oversampling wiggle pattern, a reliable fit was not achieved for this line.
[c] Due to the proximity of the $H_2$ 0-0 S(7) emission line, there is potential for contamination of [Mg VII]$_{5.503\mu m}$ emission.
[d] Jet cavity power within our deprojected 400 pc nuclear apertures estimated via L. Bîrzan et al. (2008, Equation (16)). The scatter for the 1.4 GHz jet cavity power relation is 0.85 dex.
[e] Excitation temperature is derived using extinction-corrected line flux. Reported errors correspond to the standard deviation obtained from 1000 Monte Carlo realizations, incorporating the flux uncertainties.
[f] LTE modeling and associated parameters are derived using extinction-corrected line flux. For LTE parameters, the error presented represents the fit error combined in quadrature with the standard deviation obtained from 1000 Monte Carlo realizations incorporating the flux uncertainties.

with higher ionized outflow rates. As targets within this sample are generally of similar bolometric luminosity (see Table 1), and with all things being equal, AGN photoionization is likely insufficient to explain this difference. It is possible that the strength of geometric coupling between the ionization cone and the circumnuclear disk (e.g., C. Ramos Almeida et al. 2022) may vary between objects, and targets with stronger coupling are more significantly impacted. Stronger disk–ionization cone coupling could result in more direct radiative warming of the molecular disk and have a higher potential for outflow-induced shocks.

As a result, these objects may present higher gas temperatures, stronger correlations between $H_2$ excitation and [Fe II]$_{5.34\mu m}$ emission, and more efficient mass loading, thereby bolstering the ionized outflow rate. Estimated column densities of warm $H_2$ ($T > 200$ K) from the SPL-LTE model fit also appear to show some positive correlation with ionized outflow rate, with the exception of ESO 137-G034 (interestingly, the object with the lowest bolometric luminosity), which presents a lower column density. In the case of NGC 5506 and NGC 5728, this could be the result of the AGN warming cold molecular gas in the nuclear region, resulting in an increased column density of warm/hot gas, an explanation consistent with the nuclear deficiency of cold molecular gas observed by S. García-Burillo et al. (2021, 2024) for these objects. It is possible that in the case of ESO 137-G034, AGN activity has cleared the nuclear region of some material, resulting in a lower overall column density of warm $H_2$.

Our interpretation that shock heating from outflow activity, scaling with the strength of outflow–disk coupling, is congruent with the results of previous studies that have provided evidence for AGN ionized outflow behavior to correlate with potential coupling. Notably, T. S. Bergmann (2012, and references therein) highlighted evidence that mass loading is necessary to explain the tendency of ionized outflow to be orders of magnitude larger than the mass accretion rate. F. Müller-Sánchez et al. (2011), using a sample of seven Seyferts (types 1.5 and 2), showed an anticorrelation between the half-opening angle of the outflow and both the molecular gas mass in the central 60 pc ($r < 30$ pc), as well as an anticorrelation between the half-opening angle of the outflow and the maximum outflow velocity. A broader opening angle of the ionization cone may increase the likelihood of outflow–disk coupling and thereby entrain molecular gas in the outflow and decrease the outflow velocity.

### 4.2. [Fe II]$_{5.34\mu m}$/[Ar II]$_{6.99\mu m}$ and Ionized Mass Outflow Rate

As discussed in Section 3.1, enhancement of [Fe II]$_{5.34\mu m}$ emission relative to [Ar II]$_{6.99\mu m}$ could identify the presence of

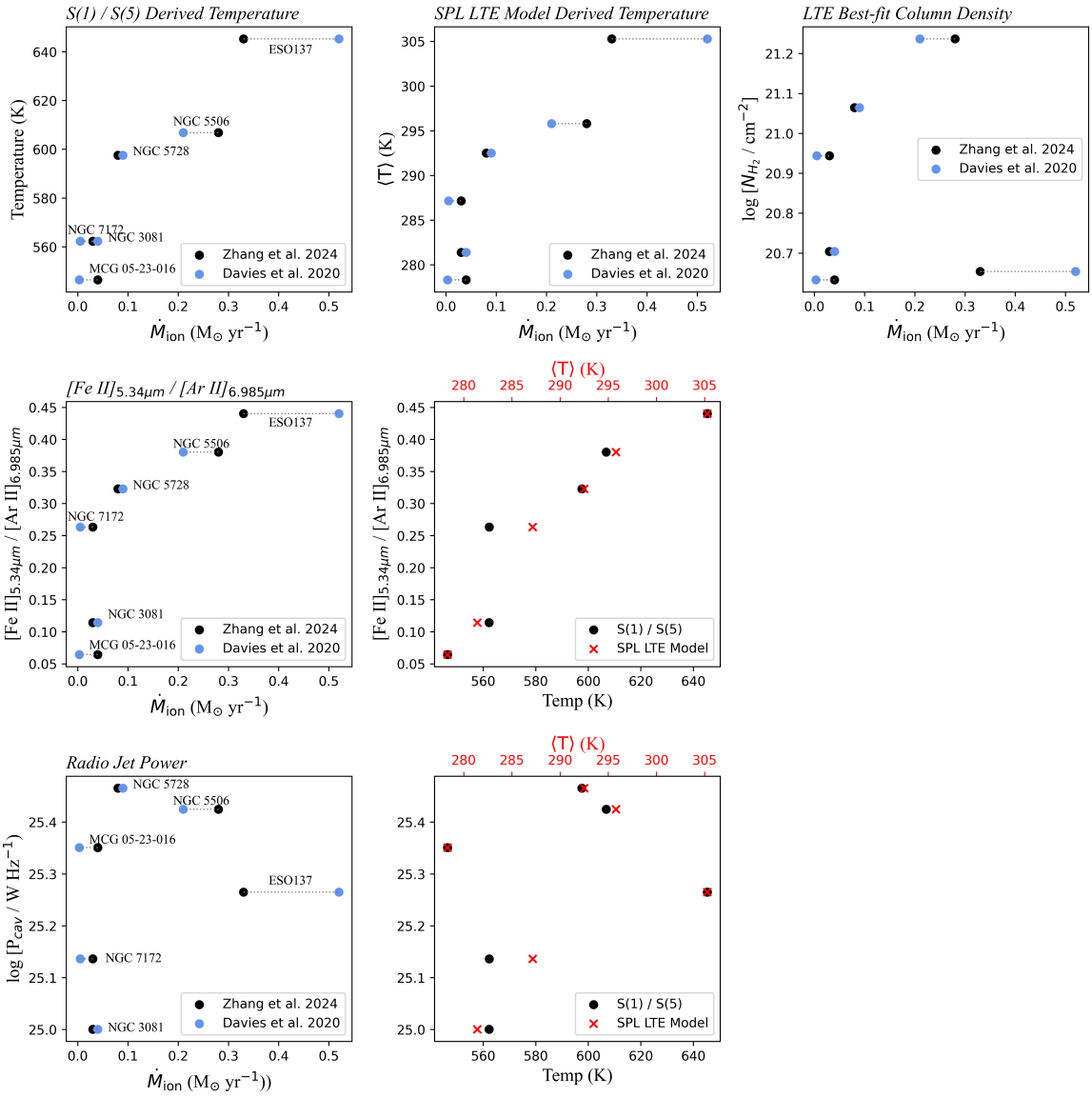


**Figure 5.** Top row panels: from left to right: $H_2$ 0-0 S(1)/S(5) derived temperature, LTE model derived temperature expectation value for the deprojected 400 pc nuclear apertures, and the LTE model derived column density vs. ionized mass outflow rates estimated by R. Davies et al. (2020) and L. Zhang et al. (2024). Middle row panels: the left panel presents the measured line ratio [Fe II]$_{5.34\mu m}$/[Ar II]$_{6.99\mu m}$ for the deprojected 400 pc nuclear apertures vs. ionized outflow rates estimated by R. Davies et al. (2020) and L. Zhang et al. (2024) and the right panel depicts [Fe II]$_{5.34\mu m}$/[Ar II]$_{6.99\mu m}$ vs. the molecular gas temperature estimated from the LTE model (top axis) and derived from the $H_2$ 0-0 S(5)/S(1) line ratio (bottom axis). Bottom row panels: estimated radio jet cavity power vs. ionized outflow rate. Associated errors with quantities are included in Table 2.

potential shocks. Figure 5 (center panels) presents measured [Fe II]$_{5.34\mu m}$/[Ar II]$_{6.99\mu m}$ for our central nuclear apertures. We report enhancement of [Fe II]$_{5.34\mu m}$/[Ar II]$_{6.99\mu m}$ to correlate positively with the ionized outflow rate as well as the estimated molecular gas temperature of the nuclear region. One explanation for this enhancement of [Fe II]$_{5.34\mu m}$ could be that dust destruction from shocks induced by disk-cone coupling, promoting mass loading of outflows and providing additional excitation energy to molecular gas. However, as discussed in Section 3.2, this interpretation comes with the caveat that theoretical models (L. Zhang et al. 2025) have suggested fast radiative shocks to yield higher ratios ([Fe II]$_{5.34\mu m}$/[Ar II]$_{6.99\mu m}$ $>$ 10) than observed here. Our observations are therefore consistent with AGN photoionization as the dominant excitation mechanism. As a result, we suspect that photoionization is the dominant excitation mechanism in the nuclear region of these Seyferts and that while the enhanced [Fe II]$_{5.34\mu m}$ may indicate shocked regions, this excitation mechanism is a less significant contributor. It is also possible that iron is somehow enhanced due to some alternative radiative process resulting in dust destruction. Regardless, the positive scaling observed between this line ratio and temperature, both derived from our SPL-LTE model and the $H_2$ 0-0 S(1)/S(5) line ratio, leads us to suspect that the mechanism driving this enhancement is likely shared by the $H_2$ excitation.

### 4.3. Jet Power and Ionized Mass Outflow Rate

From the available radio data (Figure 2) and assuming a power-law spectrum ($S_\nu \propto \nu^{-\alpha}$; with $\alpha = 0.7$), we compute the 1.4 GHz monochromatic radio luminosity and the radio jet cavity power ($P_{cav}$, via L. Bîrzan et al. 2008, Equation (16))

within the deprojected central 400 pc region of each target (Table 2). Figure 5 (bottom panels) depicts the estimated jet cavity power compared to the ionized outflow rate and estimated $H_2$ temperature. We do not observe a strong correlation between the ionized outflow rate or the molecular gas temperature and estimated jet power in our sample. While there is degeneracy in the mechanisms warming molecular gas and potentially inducing shocks within the nuclear region (e.g., outflow components, such as winds, jets etc.), we interpret this as evidence that while radio jets may be contributing to warming of the molecular gas and potentially inducing shocks, additional mechanisms are required to explain the correlation between the ionized mass outflow rate and both the molecular gas temperature and [Fe II]$_{5.34\mu m}$/[Ar II]$_{6.99\mu m}$ ratio of the nuclear region. We find the interpretation that ionization cone–disk coupling, and on smaller scales shocks, are driving the warming of the nuclear molecular gas and promoting mass loading of the ionized outflow to be a plausible explanation.

## 5. Summary

We have investigated the excitation of molecular gas within the deprojected central 400 pc region ($r < 200$ pc) as it relates to the observed ionized mass outflow rates estimated by R. Davies et al. (2020) and L. Zhang et al. (2024). Our analysis suggests the presence of shock excitation of the molecular gas to correlate with the observed ionized outflow rate. As part of this work, we report the following:

1. We observe the $H_2$ temperature distribution to be more strongly spatially correlated with [Fe II]$_{5.34\mu m}$ emission (a tracer of potential shocks) for the three targets in the sample with the highest measured ionized outflow rates. We report the SDC and $\rho$ between the $H_2$ temperature and [Fe II]$_{5.34\mu m}$ emission distribution to scale positively with the ionized outflow rate, and by extension, nuclear molecular gas temperature.
2. Based on SPL-LTE modeling of the S(1)–S(8) lines, we find the $H_2$ temperature in the central 400 pc to positively correlate with the ionized mass outflow rate, suggesting that higher excitation temperatures are associated with higher outflow rates. This observation is further corroborated by estimating the average gas excitation temperature via the $H_2$ 0-0 S(1)/S(5) line ratio.
3. We report observing enhanced [Fe II]$_{5.34\mu m}$/[Ar II]$_{6.99\mu m}$ in regions co-spatial with the ionization cone. In addition, we report the measured [Fe II]$_{5.34\mu m}$/[Ar II]$_{6.99\mu m}$ of the central 400 pc ($r < 200$ pc) nuclear region to scale positively with both ionized outflow rate and estimated molecular gas temperature, potentially indicative of shock-induced dust destruction and $H_2$ excitation.
4. We do not observe the estimated radio jet cavity power of the central 400 pc ($r < 200$ pc) nuclear region to strongly correlate with ionized mass outflow rate or nuclear molecular gas temperature of the sample.

We take the preceding points as evidence of AGN ionization cone and outflow interactions with the rotating molecular disk. The impact of coupled ionization cone and potentially outflow-induced shock heating appears to correlate with the ionized gas mass outflow rates. By extension, this may suggest that geometrical coupling between the ionization bicone and the circumnuclear disk scales with the outflow rate. This supports the interpretation that the observed ionized outflow rate is bolstered by mass loading, as targets with higher observed ionized outflow rates show evidence of outflow–disk interactions. We therefore propose that AGN feedback may well be a geometric problem to solve as much as an energetic one.

## Acknowledgments

We thank the referee for the insightful comments, which have resulted in an improved manuscript. This research utilized the unique and powerful tools included within Astropy, a community-developed Python package (T. P. Robitaille et al. 2013). We thank Raffaella Morganti for kindly providing the 8 GHz ATCA radio data for ESO 137-G034. This work is based on observations with the NASA/ESA/CSA JWST obtained from MAST at the Space Telescope Science Institute, which is operated by the Association of Universities for Research in Astronomy, Incorporated, under NASA contract No. NAS5-03127. Support for Program No. JWST- GO-01670 was provided through a grant from the STScI under NASA contract No. NAS5-03127. The specific observations analyzed can be accessed via DOI: 10.17909/c9wa-dx20.

D.D., L.Z., C.P., and E.K.S.H. acknowledge the support under a grant from the Space Telescope Science Institute (ID: JWST-GO-01670). D.D. and E.K.S.H. acknowledge support from the NASA Astrophysics Data Analysis Program (22-ADAP22-0173). M.P.S. acknowledges support under grant Nos. RYC2021-033094-I, CNS2023-145506, and PID2023-146667NB-I00 funded by MCIN/AEI/10.13039/5011000-11033 and the European Union NextGenerationEU/PRTR. A.A.H. and L.H.M. acknowledge support under grant No. PID2021-124665NB-I00 funded by MCIN/AEI/10.13039/501100011033 and by ERDF A way of making Europe. E.B. acknowledges support from the Spanish grant Nos. PID2022-138621NB-I00 and PID2021-123417OB-I00, funded by MCIN/AEI/10.13039/501100011033/FEDER, EU. C.R.A. and A.A. acknowledge support from the Agencia Estatal de Investigación of the Ministerio de Ciencia, Innovación y Universidades (MCIU/AEI) under the grant "Tracking active galactic nuclei feedback from parsec to kiloparsec scales," with reference PID2022-141105NB-I00 and the European Regional Development Fund (ERDF). A.A. also acknowledges support from the European Union (WIDERA ExGal-Twin, GA 101158446). S.G.B. and F.E. acknowledge support from the Spanish grant No. PID2022-138560NB-I00, funded by MCIN/AEI/10.13039/501100011033/FEDER, EU. I.G.B. is supported by the Programa Atracción de Talento Investigador "César Nombela" via grant No. 2023-T1/TEC-29030 funded by the Community of Madrid. D.E.A. is supported by the "Becas Estancias Posdoctorales por México" EPM(1) 2024 (CVU: 592884) program of SECIHTI and acknowledges financial support from PAPIIT UNAM IN109123 and "Ciencia de Frontera" CONAHCyT CF2023-G100. S.F.H. acknowledges support through UK Research and Innovation (UKRI) under the UK government's Horizon Europe Funding Guarantee (EP/Z533920/1, selected in the 2023 ERC Advanced Grant round) and an STFC Small Award (ST/Y001656/1). I.G.B. is supported by the Programa Atracción de Talento Investigador "César Nombela" via grant No. 2023-T1/TEC-29030 funded by the Community of Madrid. C.R. acknowledges support from the SNSF Consolidator grant No. F01-13252, Fondecyt Regular grant No. 1230345, ANID BASAL project No. FB210003, and the China-Chile joint research fund. R.A.R. acknowledges the support from the

Conselho Nacional de Desenvolvimento Científico e Tecnológico (CNPq; project Nos. 303450/2022-3 and 403398/2023-1), the Coordenação de Aperfeiçoamento de Pessoal de Nível Superior (CAPES; project No. 88887.894973/2023-00), and Fundação de Amparo à Pesquisa do Estado do Rio Grande do Sul (FAPERGS; project No. 25/2551-0002765-9). OG-M acknowledges financial support from the SECIHTI project Ciencia de Frontera CF-2023-G100, UNAM/DGAPA project PAPIIT IN109123, and Estancias Sabáticas PASPA of UNAM/DGAPA.

*Facility:* JWST (MIRI).

*Software:* astropy (T. P. Robitaille et al. 2013).

## Appendix

### A.1. Evidence for AGN Wind Interactions

Here, we provide a brief overview of each target and potential evidence for coupling/AGN wind–disk interactions.

#### A.1.1. ESO 137-G034

ESO 137-G034 is a relatively face-on lenticular galaxy with a weak nuclear bar housing an obscured (Seyfert 2) AGN (NED[31]). Of the GATOS Cycle 1 Sample, this object presents the largest observed ionized outflow rate of $0.52/0.33\ M_{\odot}\ \mathrm{yr}^{-1}$ (R. Davies et al. 2020/L. Zhang et al. 2024) and the lowest bolometric luminosity $\log[L_{\mathrm{AGN}}\ \mathrm{erg\ s}^{-1}] = 43.4$ (R. Davies et al. 2020). L. Zhang et al. (2024) identified highly kinematically disturbed regions perpendicular to the ionization cone, potentially indicating shocked regions from AGN wind interactions. More recently, D. Ł. Król et al. (2026), using X-ray observations from Chandra and spectral modeling, showed that bicone emission likely results from a combination of photoionized gas and shocked plasma, suggesting AGN kinetic feedback.

#### A.1.2. NGC 5506

NGC 5506 is a peculiar edge-on spiral galaxy housing an obscured (Seyfert type 1.9/1i[32] ) AGN (S. García-Burillo et al. 2021). The ionization bicone of NGC 5506 is oriented from the northeast to the southwest and is nearly perpendicular to the disk of the galaxy. Both ionized and molecular (cool, warm, and hot) outflows have been identified in previous works (R. Davies et al. 2020; R. A. Riffel et al. 2023; F. Esposito et al. 2024; L. Zhang et al. 2024; D. E. Delaney et al. 2025). The geometry of the ionization bicone and rotational disk was modeled by T. Fischer et al. (2013), and a potential interaction between the ionization cone and disk was suggested by F. Esposito et al. (2024), who also identified cool molecular outflows using observations from the Atacama Large Millimeter/submillimeter Array (ALMA). Further, D. E. Delaney et al. (2025), using JWST MRS IFU data, identified a region of warm molecular gas entrained in the AGN outflows and concluded AGN-induced shocks are a likely excitation mechanism for the nuclear molecular gas. Additionally, L. Zhang et al. (2024) identified a kinematically disturbed region within the western portion of the disk perpendicular to the ionization bicone.

#### A.1.3. NGC 5728

NGC 5728 is a lenticular galaxy with a weak nuclear bar surrounded by a nuclear star-forming ring and hosts an obscured (Seyfert 1.9) AGN (T. T. Shimizu et al. 2019, NED). The geometry of the ionization cone, rotational disk, and multiphase gas kinematics were studied by T. T. Shimizu et al. (2019), who reported holes in the CO (2–1) emission of the rotating disk, potentially suggesting gas removal, however found the structure of the circumnuclear region to be unaffected by the AGN. Expanding on this, R. Davies et al. (2024) used JWST/MRS IFU observations to investigate $H_2$ excitation within the central kiloparsec and reported the warmest molecular gas to be present along the edges of the ionization cone, where the molecular gas kinematics are significantly disturbed. R. Davies et al. (2020) argued that the ionization cone and rotational disk are coupled, and the molecular gas of the rotational disk is shocked and kinematically disturbed as it rotates through the ionization bicone of the AGN. This kinematic disturbance is consistent with the observations of L. Zhang et al. (2024), who reported kinematically disturbed regions of ionized gas perpendicular to the direction of the ionization cone.

#### A.1.4. NGC 3081

NGC 3081 is a lenticular galaxy and is often characterized by its three outer resonance rings and an inner resonance ring, which encircles a weak nuclear bar and connects to two star-forming arms (R. Buta & G. B. Purcell 1998; P. Ferruit et al. 2000; R. J. Buta et al. 2004). S. Eguchi et al. (2011). Housed within the center of this galaxy is an obscured (Seyfert 2) AGN, which S. Eguchi et al. (2011) argued resembled a deeply buried AGN (shrouded in a very geometrically thick torus with a small opening angle; Y. Ueda et al. 2007). A. Schnorr-Müller et al. (2016) studied the gas kinematics of NGC 3081 using observations from Gemini Multi Object Spectrograph integral field spectrograph on the Gemini North telescope and presented some evidence for interaction between the disk and AGN outflows. More recently, D. E. Delaney et al. (2025) investigated the excitation of $H_2$ using JWST/MRS IFU data and found little evidence for AGN-driven shock excitation within the circumnuclear molecular gas. Circumnuclear dust, however, was studied by H. Haidar et al. (2026) of targets including NGC 3081 using JWST/MIRI imaging and found AGN illumination to be insufficient to account for extended dust emission, indicating additional heating mechanisms, such as shocks, are required to explain observations.

#### A.1.5. NGC 7172

NGC 7172 is an almost completely edge-on ($i_{\mathrm{disk}} \approx 88°$) spiral galaxy with a heavily obscured (Seyfert 2) AGN. The nucleus of NGC 7172 is obscured both by a prominent dust lane (S. Smajić et al. 2012) and surrounded by a circumnuclear star-forming ring extending up to 1.4 kpc, which was identified by A. Alonso-Herrero et al. (2023) using CO(3–2) observations from ALMA. A. Alonso-Herrero et al. (2023) also detected nonrotational motion of cold gas within the nuclear region, indicating potentially outflowing cold molecular gas. The ionization bicone of NGC 7172 is oriented nearly completely face-on and presents a wide opening angle of

[31] The NASA/IPAC Extragalactic Database (NED) is operated by the Jet Propulsion Laboratory, California Institute of Technology, under contract with the National Aeronautics and Space Administration.

[32] This object is classified as "S1i" since it shows broad Paschen lines in the infrared, according to the nomenclature of M.-P. Véron-Cetty & P. Véron (2006).

≈120° L. Hermosa-Muñoz et al. (2024). L. Hermosa-Muñoz et al. (2024) investigated the ionized gas outflows and associated feedback in NGC 7172, indicating that the ionization cone is likely weakly coupled to the rotational disk and suggested that the reported ionized outflow rate may be underestimated as a result of extinction and projection effects.

#### A.1.6. MCG-05-23-016

MCG-05-23-016 is a spiral galaxy hosting an obscured (Seyfert 2) AGN. It boasts the lowest ionized outflow rate of the GATOS Cycle 1 sample. Despite having been shown to be a gas-poor galaxy with little evidence of star formation activity and a relatively low stellar mass (D. Rosario et al. 2018), the galaxy boasts the highest bolometric luminosity ($\log[L_{\rm AGN}$ erg $s^{-1}] = 44.3$; R. Davies et al. 2020) of the GATOS Cycle 1 sample. While evidence for geometric coupling between the ionization bicone and the rotational disk or other wind interactions is limited, D. Rosario et al. (2018) noted that the spectral energy distribution of this target is consistent with dust heated purely by the AGN. MCG-05-23-016 has been shown to contain a relatively weak compact radio jet (M. Orienti & M. Prieto 2010); however, D. Esparza-Arredondo et al. (2025) found this not to be connected to the kinematics of $H_2$ gas.

### A.2. Emission Line Fitting and Map Generation

The four channels of JWST MIRI/MRS generate observations with differing scales and spatial resolutions. To compensate, in our analysis, we have resampled all data cubes to match the smallest pixel grid across the channels (0.″13). The line fitting routine employed is similar to that described in D. E. Delaney et al. (2025), in which a third-order Chebyshev polynomial fit was used to fit and subtract the local continuum, and up to two Gaussian components were used to fit the emission lines. For error analysis, for each fit, 100 noise-perturbed mock spectra were generated, the line was refit for each mock spectra, and the standard deviation of the fits was recorded as an error. Line maps have been masked such that any spaxel with flux that did not meet the signal-to-noise threshold of 3 was masked. In addition, spaxels with measured velocity or $|\sigma| > 800$ km s$^{-1}$ have been masked. Where spaxel-by-spaxel analysis was performed (i.e., temperature mapping and estimation of Dice coefficient and $\rho$), we have convolved the $H_2$ 0-0 S(5) (6.9095 $\mu$m) and [Fe II]$_{5.34\mu m}$ line maps with the FWHM of the larger PSF of the $H_2$ 0-0 S(1) (17.0346 $\mu$m) emission to match dataset resolution.

### A.3. Integrated Spectra and Population Levels

Here, we present the integrated spectra (Figure 6) from the deprojected 400 pc nuclear apertures and the resulting population levels with the best-fit SPL model (Figure 7) for each target. Nuclear apertures are 3.44 arcsec$^2$ for ESO 137-G034, 2.51 arcsec$^2$ for NGC 5506, 2.57 arcsec$^2$ for NGC 5728, 3.49 arcsec$^2$ for NGC 3081, 1.34 arcsec$^2$ for NGC 7172, and 3.58 arcsec$^2$ for MCG-05-23-016.

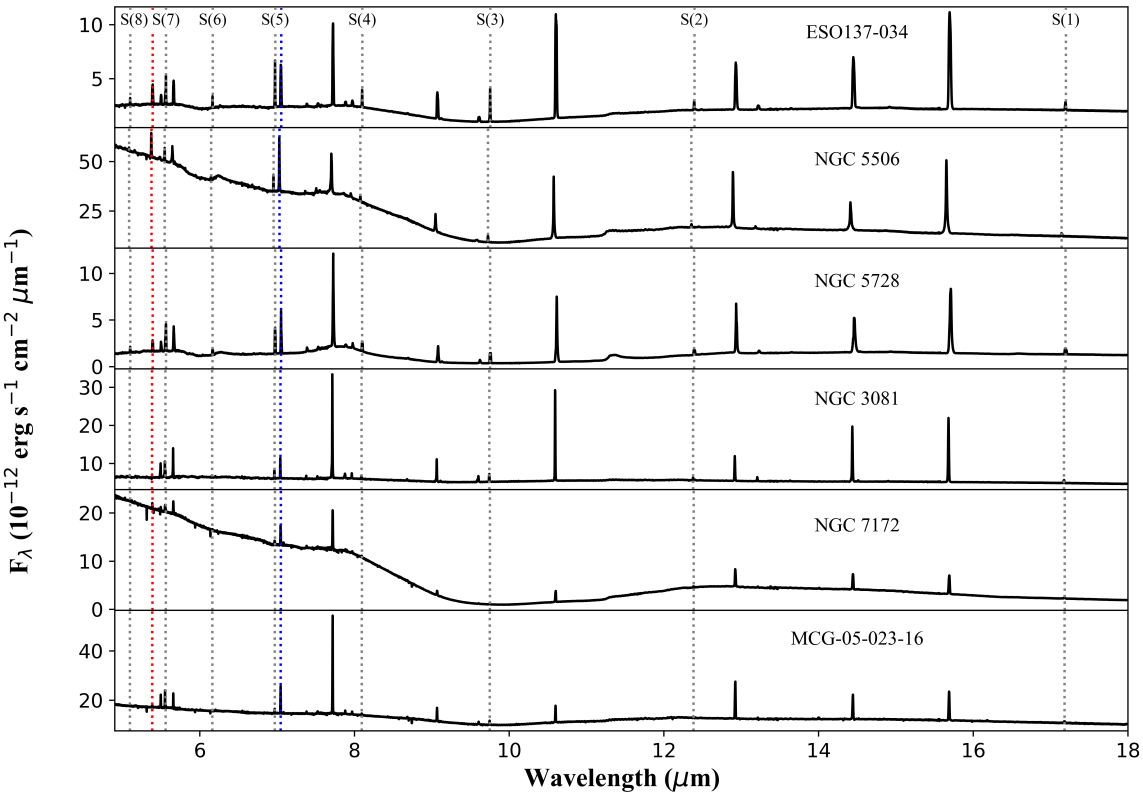


**Figure 6.** Integrated spectra extracted from the 400 pc nuclear aperture for each object at rest frame wavelength. The S(1)–S(8) rotational $H_2$ emission lines are identified by the black dotted line. The red dotted line identifies the position of the [Fe II]$_{5.34\mu m}$ emission line, and the blue dotted line identifies the [Ar II]$_{6.99\mu m}$ emission line.

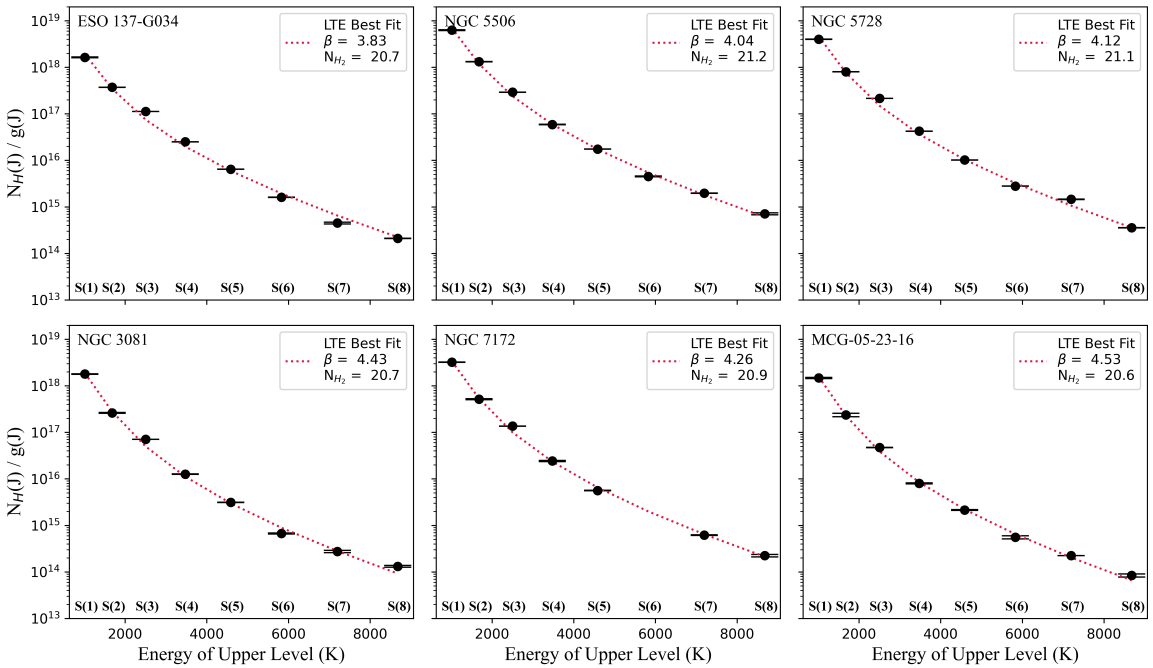


**Figure 7.** Best-fit LTE models for the S(1)–S(8) population levels. The S(7) population level was omitted from the model fit due to potential contamination by [Mg VII]$_{5.503\mu m}$ emission.

### *A.4. Extinction Corrections*

Extinction corrections were applied using the T. K. Fritz et al. (2011) infrared extinction curve, which was derived for the Galactic center using hydrogen emission lines. Extinction was estimated using the adjacent S(3) and S(4) emission line flux relative to the intrinsic line flux predicted assuming LTE, and a Boltzmann distribution at the temperature estimated via Equation (1). As the S(1) and S(5) emission experience differential absorption, we calculate the gas temperature with the extinction-corrected flux and reiterate this procedure until the computed temperature converges. Across the sample, differential reddening from the $H_2$ 0-0 S(1)–S(8) lines is generally minor, with NGC 7172 being the most significantly impacted by extinction effects. For NGC 3081, ESO 137-G034,and MCG-05-23-16, we estimate a differential reddening of 0.1 mag from the S(1)–S(8) emission. For NGC 5506 and NGC 5728, the differential reddening is 0.2 mag, and for NGC 7172, the differential reddening is 0.3 mag. The S(3) emission line is impacted significantly by the 9.7 $\mu$m silicate absorption feature. The ratio $F_{S(3)}/F_{S(1)}$ is adjusted by a factor of 1.5 for ESO 137-G034, 2.5 for NGC 5506, 2.4 for NGC 5728, 1.6 for NGC 3081, 5.3 for NGC 7172, and 1.4 for MCG-05-23-016. We spot check our extinction correction via the S(3) associated population level (Figure 7). As the resultant population level appears reasonable, we conclude that our extinction correction is valid.

## ORCID iDs

Daniel E. Delaney https://orcid.org/0009-0007-6992-2555
Erin K. S. Hicks https://orcid.org/0000-0002-4457-5733
Lulu Zhang https://orcid.org/0000-0003-4937-9077
Ric Davies https://orcid.org/0000-0003-4949-7217
Chris Packham https://orcid.org/0000-0001-7827-5758
Rogemar A. Riffel https://orcid.org/0000-0003-0483-3723
Miguel Pereira Santaella https://orcid.org/0000-0002-4005-9619
Enrica Bellocchi https://orcid.org/0000-0001-9791-4228
Nancy A. Levenson https://orcid.org/0000-0003-4209-639X
Steph Campbell https://orcid.org/0000-0001-9520-7765
David J. Rosario https://orcid.org/0000-0002-0001-3587
Houda Haidar https://orcid.org/0000-0002-3741-6136
Cristina Ramos Almeida https://orcid.org/0000-0001-8353-649X
Anelise Audibert https://orcid.org/0000-0003-3589-3294
Claudio Ricci https://orcid.org/0000-0001-5231-2645
Laura Hermosa Muñoz https://orcid.org/0000-0002-9610-0123
Francoise Combes https://orcid.org/0000-0003-2658-7893
Almudena Alonso-Herrero https://orcid.org/0000-0001-6794-2519
Santiago García-Burillo https://orcid.org/0000-0003-0444-6897
Federico Esposito https://orcid.org/0000-0002-5775-6285
Ismael García-Bernete https://orcid.org/0000-0002-9627-5281
Taro Shimizu https://orcid.org/0000-0002-2125-4670
Martin Ward https://orcid.org/0000-0003-1810-0889
Omaira González-Martín https://orcid.org/0000-0002-2356-8358
Alvaro Labiano https://orcid.org/0000-0002-0690-8824
Oscar Veenema https://orcid.org/0009-0009-0466-9223
Enrique Lopez-Rodriguez https://orcid.org/0000-0001-5357-6538
Dimitra Rigopoulou https://orcid.org/0000-0001-6854-7545
Marko Stalevski https://orcid.org/0000-0001-5146-8330
Sebastian F. Hönig https://orcid.org/0000-0002-6353-1111
Donaji Esparza-Arredondo https://orcid.org/0000-0001-8042-9867
Takuma Izumi https://orcid.org/0000-0001-9452-0813
Lindsay Fuller https://orcid.org/0000-0003-4809-6147

## References


Alonso-Herrero, A., García-Burillo, S., Pereira-Santaella, M., et al. 2019, A&A, 628, A65
Alonso-Herrero, A., Muñoz, L. H., Labiano, A., et al. 2024, A&A, 690, A95
Alonso-Herrero, A., Muñoz, L., Labiano, A., et al. 2025, A&A, 699, A34
Alonso-Herrero, A., García-Burillo, S., Pereira-Santaella, M., et al. 2023, A&A, 675, A88
Amayo, A., Delgado-Inglada, G., & Stasińska, G. 2021, MNRAS, 505, 2361
Antonucci, R. 1993, ARA&A, 31, 473
Argyriou, I., Glasse, A., Law, D. R., et al. 2023, A&A, 675, A111
Audibert, A., Almeida, C. R., García-Burillo, S., et al. 2023, A&A, 671, L12
Baumgartner, W., Tueller, J., Markwardt, C., et al. 2013, ApJS, 207, 19
Bergmann, T. S. 2012, ASPC, 460, 133
Bessiere, P. S., & Ramos Almeida, C. 2022, MNRAS, 512, L54
Bîrzan, L., McNamara, B., Nulsen, P., Carilli, C., & Wise, M. 2008, ApJ, 686, 859
Burton, M. G., Hollenbach, D., & Tielens, A. 1992, ApJ, 399, 563
Burtscher, L., Davies, R. I., Shimizu, T., et al. 2021, A&A, 654, A132
Buta, R., & Purcell, G. B. 1998, AJ, 115, 484
Buta, R. J., Byrd, G. G., & Freeman, T. 2004, AJ, 127, 1982
Caglar, T., Burtscher, L., Brandl, B., et al. 2020, A&A, 634, A114
Cicone, C., Maiolino, R., Sturm, E., et al. 2014, A&A, 562, A21
Crenshaw, D., Kraemer, S., Schmitt, H., et al. 2010, AJ, 139, 871
Crenshaw, D. M., & Kraemer, S. B. 2012, ApJ, 753, 75
Davies, R., Baron, D., Shimizu, T., et al. 2020, MNRAS, 498, 4150
Davies, R., Maciejewski, W., Hicks, E., et al. 2014, ApJ, 792, 101
Davies, R., Sánchez, F. M., Genzel, R., et al. 2007, ApJ, 671, 1388
Davies, R., Shimizu, T., Pereira-Santaella, M., et al. 2024, A&A, 689, A263
Davies, R. I., Burtscher, L., Rosario, D., et al. 2015, ApJ, 806, 127
de Arriba, L. P., Alonso-Herrero, A., García-Burillo, S., et al. 2023, A&A, 675, A58
Delaney, D. E., Hicks, E. K., Zhang, L., et al. 2025, ApJ, 993, 217
Eguchi, S., Ueda, Y., Awaki, H., et al. 2011, ApJ, 729, 31
Ellison, S. L., Sánchez, S. F., Ibarra-Medel, H., et al. 2018, MNRAS, 474, 2039
Esparza-Arredondo, D., Almeida, C. R., Audibert, A., et al. 2025, A&A, 693, A174
Esposito, F., Alonso-Herrero, A., García-Burillo, S., et al. 2024, A&A, 686, A46
Esquej, P., Alonso-Herrero, A., González-Martín, O., et al. 2013, ApJ, 780, 86
Fabian, A. C. 2012, ARA&A, 50, 455
Ferruit, P., Wilson, A. S., & Mulchaey, J. 2000, ApJS, 128, 139
Fischer, T., Crenshaw, D., Kraemer, S., & Schmitt, H. 2013, ApJS, 209, 1
Fischer, T., Crenshaw, D., Kraemer, S., et al. 2011, ApJ, 727, 71
Fischer, T., Smith, K. L., Kraemer, S., et al. 2019, ApJ, 887, 200
Fischer, T. C., Johnson, M. C., Secrest, N. J., Crenshaw, D. M., & Kraemer, S. B. 2023, ApJ, 953, 87
Fischer, T. C., Kraemer, S., Schmitt, H. R., et al. 2018, ApJ, 856, 102
Fischer, T. C., Machuca, C., Diniz, M. R., et al. 2016, ApJ, 834, 30
Fritz, T. K., Gillessen, S., Dodds-Eden, K., et al. 2011, ApJ, 737, 73
Gallimore, J. F., Elitzur, M., Maiolino, R., et al. 2016, ApJL, 829, L7
García-Bernete, I., Alonso-Herrero, A., García-Burillo, S., et al. 2021, A&A, 645, A21
García-Bernete, I., Alonso-Herrero, A., Rigopoulou, D., et al. 2024, A&A, 681, L7
García-Bernete, I., Rigopoulou, D., Alonso-Herrero, A., et al. 2022, A&A, 666, L5
García-Burillo, S., Alonso-Herrero, A., Almeida, C. R., et al. 2021, A&A, 652, A98
García-Burillo, S., Combes, F., Almeida, C. R., et al. 2016, ApJL, 823, L12
García-Burillo, S., Combes, F., Almeida, C. R., et al. 2019, A&A, 632, A61
García-Burillo, S., Combes, F., Usero, A., et al. 2014, A&A, 567, A125
García-Burillo, S., Hicks, E., Alonso-Herrero, A., et al. 2024, A&A, 689, A347
Gardner, J. P., Mather, J. C., Abbott, R., et al. 2023, PASP, 135, 068001
Harrison, C. 2017, NatAs, 1, 0165
Haidar, H., Rosario, D. J., García-Bernete, I., et al. 2026, MNRAS, 546, stag069
Harrison, C., Costa, T., Tadhunter, C., et al. 2018, NatAs, 2, 198
Harrison, C. M., & Ramos Almeida, C. 2024, Galax, 12, 17
Hermosa-Muñoz, L., Alonso-Herrero, A., Pereira-Santaella, M., et al. 2024, A&A, 690, A350
Hickox, R. C., & Alexander, D. M. 2018, ARA&A, 56, 625
Holden, L. R., Tadhunter, C., Audibert, A., et al. 2024, MNRAS, 530, 446
Hopkins, P. F., Hernquist, L., Cox, T. J., et al. 2005, ApJ, 630, 705
Hunt, L., Draine, B., Navarro, M., et al. 2025, ApJ, 993, 84
Imanishi, M., Nakanishi, K., Izumi, T., & Wada, K. 2018, ApJL, 853, L25
Imanishi, M., Vollmer, B., Hagiwara, Y., et al. 2025, ApJ, 995, 211
Impellizzeri, C. V., Gallimore, J. F., Baum, S. A., et al. 2019, ApJL, 884, L28
Jenkins, E. B. 2009, ApJ, 700, 1299
Jones, A., Tielens, A., & Hollenbach, D. 1996, ApJ, 469, 740
Jones, A., Tielens, A., Hollenbach, D., & McKee, C. 1994, ApJ, 433, 797
Khalatyan, A., Cattaneo, A., Schramm, M., et al. 2008, MNRAS, 387, 13
Koo, B.-C., Raymond, J. C., & Kim, H.-J. 2016, JKAS, 49, 109
Król, D. Ł., Fabbiano, G., Elvis, M., et al. 2026, ApJ, 998, 135
Lien, A. Y., Krimm, H., Markwardt, C., et al. 2025, ApJ, 989, 161
Lodders, K. 2003, ApJ, 591, 1220
Ma, J., Elvis, M., Fabbiano, G., et al. 2020, ApJ, 900, 164
Maiolino, R., Russell, H., Fabian, A. C., et al. 2017, Natur, 544, 202
Molina, J., Ho, L. C., Wang, R., et al. 2023, ApJ, 944, 30
Morganti, R., Tsvetanov, Z., Gallimore, J., & Allen, M. 1999, A&AS, 137, 457
Müller-Sánchez, F., Prieto, M., Hicks, E., et al. 2011, ApJ, 739, 69
NRAO/VLA Archive Survey 2007, NRAO/VLA Archive Survey Image, https://data.nrao.edu/portal/#/
Ogle, P., Antonucci, R., Appleton, P., & Whysong, D. 2007, ApJ, 668, 699
Orienti, M., & Prieto, M. 2010, MNRAS, 401, 2599
Pereira-Santaella, M., Álvarez-Márquez, J., García-Bernete, I., et al. 2022, A&A, 665, L11
Pereira-Santaella, M., García-Bernete, I., González-Alfonso, E., et al. 2024, A&A, 685, L13
Pereira-Santaella, M., Spinoglio, L., van der Werf, P. P., & López, J. P. 2014, A&A, 566, A49
Ramos Almeida, C., Bischetti, M., García-Burillo, S., et al. 2022, A&A, 658, A155
Ramos Almeida, C., & Ricci, C. 2017, NatAs, 1, 679
Rieke, G. H., Wright, G., Böker, T., et al. 2015, PASP, 127, 584
Riffel, R. A., Colina, L., Costa-Souza, J. H., et al. 2026, A&A, 705, A59
Riffel, R. A., Souza-Oliveira, G. L., Costa-Souza, J. H., et al. 2025, ApJ, 982, 69
Riffel, R. A., Storchi-Bergmann, T., Riffel, R., et al. 2023, MNRAS, 521, 1832
Rigby, J., Perrin, M., McElwain, M., et al. 2023, PASP, 135, 048001
Robitaille, T. P., Tollerud, E. J., Greenfield, P., et al. 2013, A&A, 558, A33
Rosario, D., Burtscher, L., Davies, R. I., et al. 2018, MNRAS, 473, 5658
Ruschel-Dutra, D., Storchi-Bergmann, T., Schnorr-Müller, A., et al. 2021, MNRAS, 507, 74
Schmitt, H., Ulvestad, J., Antonucci, R., & Kinney, A. 2001, ApJS, 132, 199
Schnorr-Müller, A., Storchi-Bergmann, T., Robinson, A., Lena, D., & Nagar, N. M. 2016, MNRAS, 457, 972
Shimizu, T. T., Davies, R., Lutz, D., et al. 2019, MNRAS, 490, 5860
Silk, J., & Rees, M. J. 1998, A&A, 331, L1
Smajić, S., Fischer, S., Zuther, J., & Eckart, A. 2012, A&A, 544, A105
Sofia, U. J., & Jenkins, E. B. 1998, ApJ, 499, 951
Tielens, A., McKee, C., Seab, C., & Hollenbach, D. 1994, ApJ, 431, 321
Togi, A., & Smith, J. 2016, ApJ, 830, 18
Ueda, Y., Eguchi, S., Terashima, Y., et al. 2007, ApJ, 664, L79
Urry, C. M., & Padovani, P. 1995, PASP, 107, 803
Veilleux, S., Cecil, G., & Bland-Hawthorn, J. 2005, ARA&A, 43, 769
Veilleux, S., Meléndez, M., Sturm, E., et al. 2013, ApJ, 776, 27
Venturi, G., Cresci, G., Marconi, A., et al. 2021, A&A, 648, A17
Verma, A., Lutz, D., Sturm, E., et al. 2003, A&A, 403, 829
Véron-Cetty, M.-P., & Véron, P. 2006, A&A, 455, 773
Wada, K. 2012, ApJ, 758, 66
Wells, M., Pel, J.-W., Glasse, A., et al. 2015, PASP, 127, 646
Zakamska, N. L., & Greene, J. E. 2014, MNRAS, 442, 784
Zhang, L., Davies, R. I., Packham, C., et al. 2025, ApJS, 280, 65
Zhang, L., & Ho, L. C. 2023, ApJL, 953, L9
Zhang, L., Packham, C., Hicks, E. K., et al. 2024, ApJ, 974, 195
Zubovas, K., & Nardini, E. 2020, MNRAS, 498, 3633